Removal of residual compositions by powder engineering for high efficiency formamidinium-based perovskite solar cells with operation lifetime over 2000 hours

Guoqing Tong[a], Dae-Yong Son[a], Luis K. Ono[a], Hyung-Been Kang[b], Sisi He[a], Longbin Qiu[a], Hui Zhang[a], Yuqiang Liu[a], Jeremy Hieulle[a], Yabing Qi[a,*]

[a]Energy Materials and Surface Sciences Unit (EMSSU), Okinawa Institute of Science and Technology Graduate University (OIST), 1919-1 Tancha, Onna-son, Kunigami-gun, Okinawa 904-0495, Japan

[b]Engineering Section, Okinawa Institute of Science and Technology Graduate University (OIST), 1919-1 Tancha, Onna-son, Okinawa 904-0495, Japan

*Corresponding author: Yabing Qi, E-mail: Yabing.Qi@OIST.jp

ABSTRACT:

Defects have a detrimental effect on efficiency and stability of perovskite solar cells (PSCs) due to the structural imperfections and/or extrinsic impurities in the perovskite films. Here, we propose to use a pre-synthesized crystalline perovskite with perfect stoichiometry to control and lower the density of defects from precursors by the powder engineering method. Compared with raw materials (i.e., PbI_2 and FAI) based perovskites, the average efficiency of the PSCs fabricated based on these pre-synthesized perovskite precursors increased from 18.62% to 19.85%. Moreover, the unwanted intermediate chemical compositions (i.e., the unreacted phases and residual solvent) in the raw material-based perovskite films were significantly reduced in the pre-synthesized δ-$FAPbI_3$ and α-$FAPbI_3$ perovskites according to the secondary ion mass spectroscopy depth profiling data. Finally, we obtained the champion efficiency of 22.76% for α-$FAPbI_3$ and 23.05% for $FAPb(I_{0.9}Br_{0.1})_3$ based PSCs. Long-term operational stability of encapsulated $FAPb(I_{0.9}Br_{0.1})_3$ based PSCs showed a slow decay and maintained the efficiency about 88% after 1200 hours (T_{80} > 2000 h). Furthermore,

a proof-of-concept integrated perovskite solar module-lithium ion battery-light-emitting diode device was demonstrated.

Keywords: perovskite solar cells, powder engineering, solar modules, efficiency, operational stability

1. Introduction

The two-pioneering works on lead halide perovskite solar cells (PSCs) in 2009 and 2011 give rise to tremendous research activities on this class of materials worldwide[1-2]. Up to now, an outstanding power-conversion-efficiency (PCE) of 25.5% has recently been achieved, which is highly competitive even when compared with well-established photovoltaic technologies such as those based on Si (a record PCE of 26.7%) and CdTe (21-22%)[3-4]. Formamidinium lead iodide ($FAPbI_3$), as a member in the perovskite family, has been widely investigated because of its favorable band gap (~1.48 eV), which is close to the optimal value of Shockley-Queisser optimum (i.e., 1.34 eV)[5-7]. However, the phase transition from the black α-$FAPbI_3$ phase to non-photoactive isomer δ-$FAPbI_3$ phase in ambient conditions makes it difficult to achieve a high efficiency (over 23%) and stability (more than 1000 hours) (Table S1) simultaneously[6-8]. Although several strategies have been developed to improve the phase stability of $FAPbI_3$ based PSCs, such as cation mixing[7, 9-10], bromide substitution[11-12], surface treatment[6, 13-15] and additive engineering[16-17], the stability still lags behind those of the established photovoltaics. In addition, the

polycrystalline nature of $FAPbI_3$ perovskite films is highly dependent on the precursor quality. Large amounts of traps induced by structural imperfections and/or extrinsic impurities are mainly formed at the surfaces and grain boundaries, which is often associated with the variations in device performance[18-20]. To overcome it, incorporation of excess of serval precursor materials e.g., PbI_2 and/or organic halides (MAI, MCl) is proposed to improve the solar cell performance. The excess PbI_2 is proposed to be beneficial in improving the efficiency of perovskite solar cells, because it can passivate defects in perovskite films[21-23]. But excess PbI_2 and its degradation products (e.g., Pb and I_2) can also lead to accelerated degradation of the perovskite layer[24-26]. Additionally, excess organic halides in the perovskite films can improve the crystallinity, enlarge grain size and provide a better energy level alignment, leading to an improved efficiency in final devices[27-31]. However, it is worth noting that excess organic halide sometimes will induce the formation of MA_4PbI_6, in which MAI acts as a matrix structure with embedded PbI_2[32]. Moreover, a too thick layer of MAI on the top of perovskite will lead to poorer charge transport and therefore lower solar cell performance, as demonstrated in our previous work[29]. Therefore, making a high-quality perovskite is an imperative way to achieve high efficiency and long-term stability PSCs.

Recently, perovskite single crystals have been reported and widely used in photodetectors, X-ray dector and solar cells[33-38]. The stoichiometry is close to the ideal value and defects in single crystals are several orders of magnitude lower than that in polycrystalline counterparts, which leads to high performance and stability[38-40].

For example, $MAPbI_3$ single crystal-based PSCs have shown outstanding PCEs of 21.09% and 21.9%[38-39]. However, device-incompatible solution growth conditions, complicated fabrication and low yield make the efficiency of single crystals-PSCs still inferior to the polycrystalline films PSCs and also impede their application in large-scale devices[41]. To increase the yield of perovskites, Zhang et al. reported the prey-synthesized perovskite powders, and demonstrated that the synthesis of non-stoichiometric δ-$FAPbI_3$ powder in acetonitrile could overcome the low PCE issues even using the low-grade PbI_2 precursor[42]. But a detailed investigation on the unreacted phases and residue solvent in these pre-synthesized perovskite powders is currently lacking.

Here, we present a simple powder engineering method to synthesize δ-$FAPbI_3$ and α-$FAPbI_3$ crystalline powders with a high yield, and a detailed study on the residual compositions (i.e., the unreacted phases and residue solvent) in the pre-synthesized perovskite powders, which yields key information and strategy for the further improvement of efficiency and stability. In comparison with R-$FAPbI_3$ ($FAPbI_3$ prepared by FAI and PbI_2 raw powders), the pre-synthesized δ-$FAPbI_3$ and α-$FAPbI_3$ have low trap density and lead to high performance in PSCs. In addition, secondary ion mass spectroscopy (SIMS) measurements revealed that a small amount of non-reacted or aggregated FAI (m/z=182-183) as well as the residual solvent was observed in R-$FAPbI_3$, but it decreased in the pre-synthesized δ-$FAPbI_3$ and α-$FAPbI_3$ films. Finally, we observed the highest PCE of 22.76% for α-$FAPbI_3$ and 23.05% for $FAPb(I_{0.9}Br_{0.1})_3$ based PSCs, respectively. The operational stability showed >88% at 1200 h and a decay

rate of approximately -0.01%/h with a T_{80} lifetime over 2000 h. Besides, 5 × 5 cm^2 perovskite solar modules (PSMs) were fabricated with a champion module PCE of 14.22% (active area PCE=16.01%), indicating the good scalability of this technique. Furthermore, a proof-of-concept perovskite solar module-lithium ion battery-light-emitting diode (PSM-LIB-LED) device was demonstrated to operate well by converting the light to electricity and stored in a Li battery, which can power LED under dark condition. Our work provides a simple and high yield method to synthesize highly crystalline powders, which enables fabrication of PSCs with both high PCEs and long-term operational stability.

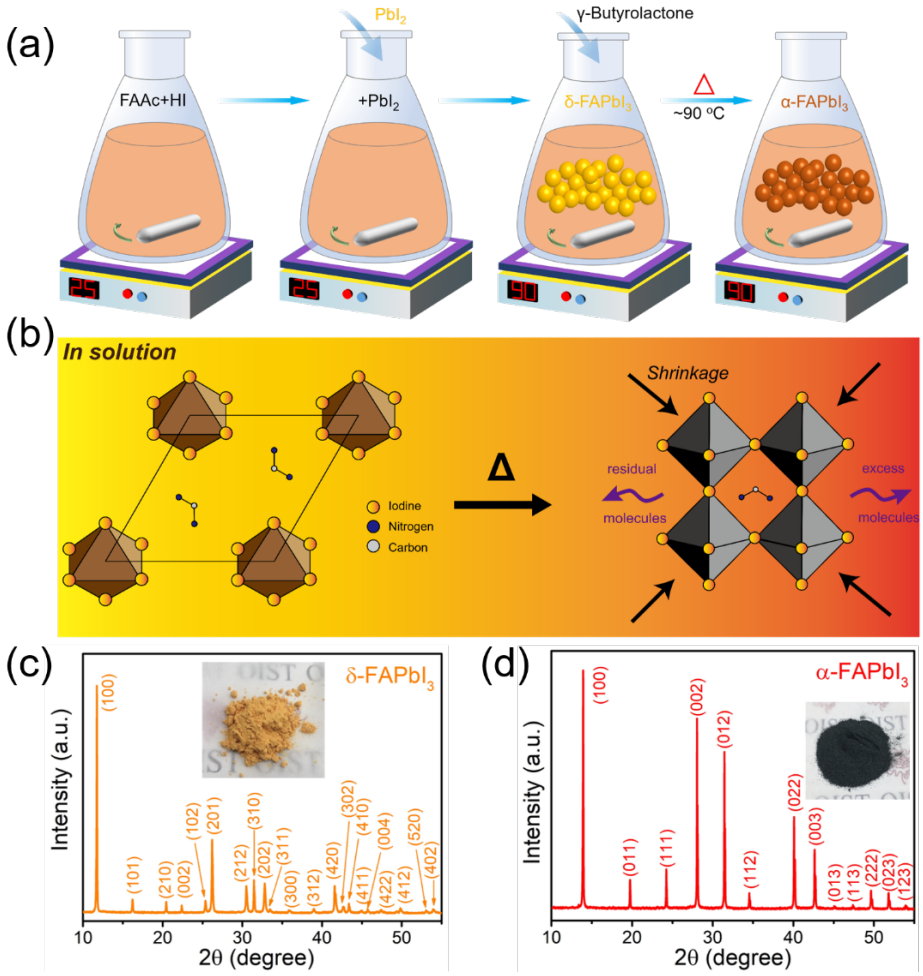

Fig. 1. (a) Schematic illustration of the synthesis pathways of phase pure δ-$FAPbI_3$ and

α-$FAPbI_3$ precursor powders; (b) Mechanism of volume shrinkage in the $FAPbI_3$ crystal structure. XRD patterns of (c) δ-$FAPbI_3$ and (d) α-$FAPbI_3$ (insets: Photographs of the synthesized powders).

2. Results and Discussion

2.1. Synthesis and characterization of pre-synthesized powders.

Fig. 1a displays a schematic drawing showing the synthesis process of δ-$FAPbI_3$ and α-$FAPbI_3$ by the powder engineering method. Formamidinium acetate (FAAc) is first slowly mixed with hydroiodic acid (HI) with a molar ratio of 1:1.1 (eq. 1). After dissolution of FAAc, PbI_2 is added into the mixed solution to form the δ-$FAPbI_3$ (eq. 2), which is confirmed by the XRD data in Fig. 1c. Once δ-$FAPbI_3$ powders were heated up to 90 ^{o}C for 1-2 hours, the slow conversion from the δ-phase to the α-phase $FAPbI_3$ was observed and the corresponding unit cell size reduced from 517 to 257 $Å^3$ (Fig. 1b, eq. 3). In this step, the remaining impurities and the unreacted precursors were then dissolved by H_2O and filtered. Inspired by the previous reports about the growth of the perovskite single crystals using γ-Butyrolactone (GBL) as solvent[43-46], which not only provides an excellent solubility of perovskites at low temperatures, but also decreases the solubility of perovskites as the temperature increases to approximately 100 ^{o}C[44, 47]. Then GBL was used as a solvent to dissolve the less stable, non-stoichiometric $FAPbI_3$ phase with dangling bonds. Similarly, the cubic phase (Pm3m) $FAPbBr_3$ perovskite powder can be synthesized as shown in Fig. S1. Finally, high powder yields of 93-95% for α-$FAPbI_3$, δ-$FAPbI_3$, respectively, and 82% for $FAPbBr_3$ are obtained by this method.

$$FAAc + I^- + H_3O^+ \rightarrow FAI + Ac^- + H_3O^+ \qquad (1)$$

$$PbI_2 + FAAc + I^- + H_3O^+ \rightarrow FAPbI_3\ (\delta) + Ac^- + H_3O^+ \qquad (2)$$

$$GBL + FAPbI_3\ (\delta) + Ac^- + H_3O^+ \xrightarrow{\Delta} FAPbI_3\ (\alpha) + GBL + Ac^- \uparrow + H_3O^+ \uparrow \qquad (3)$$

The yellow color powders of δ-$FAPbI_3$ and black color powders of α-$FAPbI_3$ (Figs. 1c and 1d, inset) were characterized by scanning electron microscopy (Fig. S2) and X-ray diffraction (XRD) to confirm the crystal structure. Rietveld refinement was performed for the XRD data (Figs. 1c-1d) using TOPAS software (Fig. S3)[48]. Refined lattice constants of α-$FAPbI_3$ (Pm-3m) are a=6.35743(5) Å (Tables S2), slightly smaller than the previously reported structure (a=6.3620(8))[49]. Refined lattice constants of δ-$FAPbI_3$ ($P6_3mc$) are a=8.67827(18) Å and c=7.9306(2) Å (Tables S3, Supporting Information). These values are slightly larger than the previously reported structure (a=8.6603(14) Å and c=7.9022(6) Å)[50]. Moreover, for both $FAPbI_3$ materials no peaks corresponding to impurity phases were detected, indicating the phase purity of these two pre-synthesized materials. Fig. S4 shows the high-resolution transmission electron microscopy (HRTEM) images of pre-synthesized δ-$FAPbI_3$ and α-$FAPbI_3$. The measured interplanar spacing of 5.44 Å and 6.48 Å for δ-$FAPbI_3$ and α-$FAPbI_3$ are assigned to the (101) and (100) crystal plane, respectively, which agrees well with the XRD data for the hexagonal and cubic phase of $FAPbI_3$, respectively. The corresponding selected area electron diffraction (SAED) patterns as shown in Figs. S4b and S4d have highly symmetrical lattice plane, which corroborates the high crystallinity of δ-$FAPbI_3$ and α-$FAPbI_3$. The diffraction spots of the SAED patterns are indexed to

the (202), (301) and (200) reflections of the hexagonal phase with the space group of $P6_3mc$ and (100) and (110) reflections of the cubic phase with the space group of Pm-3m[49].

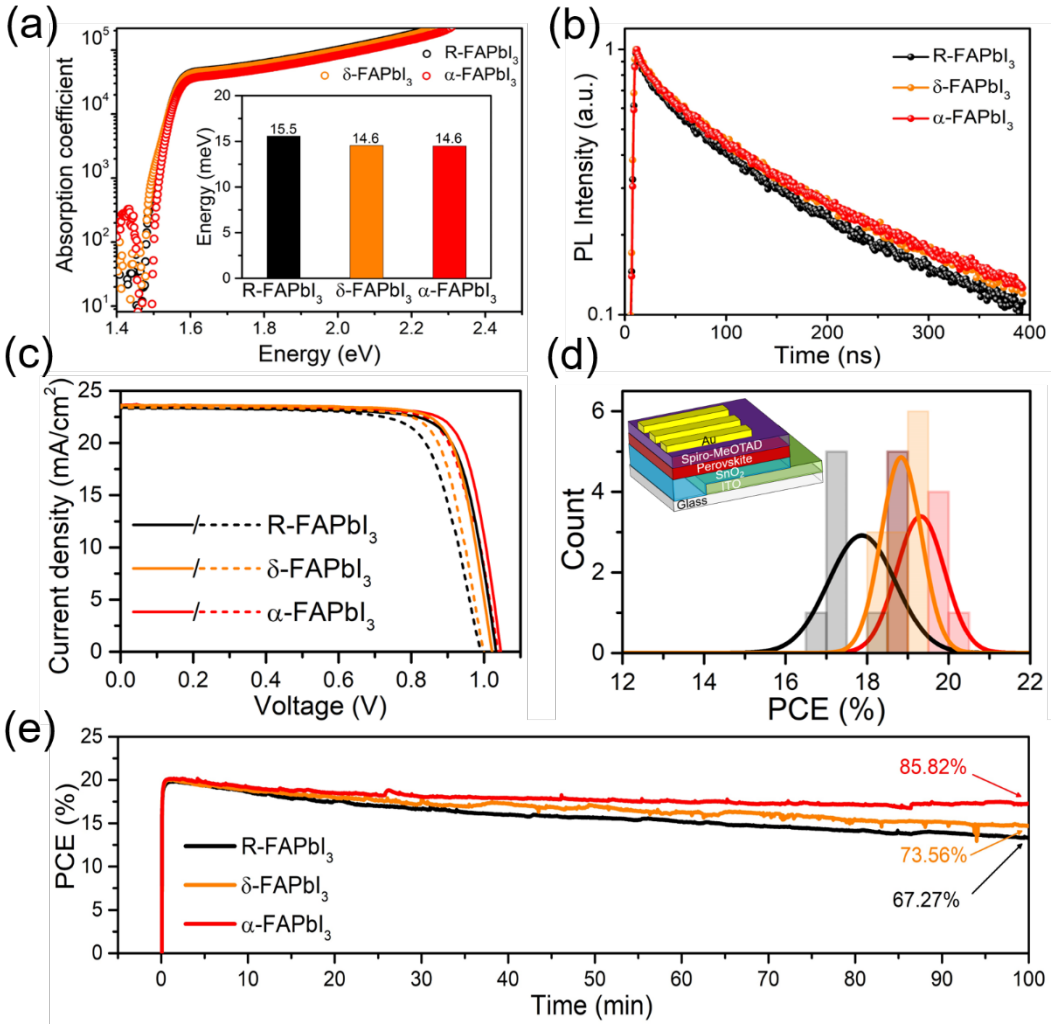

Fig. 2. (a) Absorption coefficients of the R-$FAPbI_3$, δ-$FAPbI_3$ and α-$FAPbI_3$ as a function of photon energy (inset: Calculated Urbach tail energy data); (b) TRPL of R-$FAPbI_3$, δ-$FAPbI_3$ and α-$FAPbI_3$; (c) J-V curves of R-$FAPbI_3$, δ-$FAPbI_3$ and α-$FAPbI_3$ based PSCs. Solid and dash lines correspond to the reverse and forward scan, respectively; (d) Statistical PCEs (inset: Device architecture); (e) Operational stability of R-$FAPbI_3$, δ-$FAPbI_3$ and α-$FAPbI_3$ devices under a steady voltage output and continuous illumination in ambient condition without encapsulation.

2.2. Pre-synthesized phase pure $FAPbI_3$ solid powders for PSCs.

Although the perovskite powders are synthesized using GBL as the solvent, the fast nucleation rate of the perovskite crystals during the spin-coating process can lead to a poor morphology of the perovskite film[51]. To prepare high quality perovskite films, we first dissolved the perovskite powders into the DMF/DMSO mixture solvent (More details can be found in the experimental section). Photovoltaic performance was evaluated by assembling a device as seen in Fig. 2d (inset). A compact and uniform perovskite layer with large grain sizes can enhance the light capture and reduce the leakage path in the devices (Fig. S5). We estimated the Urbach tail energy from the Tauc plot in Fig. S6. Due to the additional MACl additive, the optical gap of all series of $FAPbI_3$ could be estimated as 1.548-1.549 eV[42, 52]. Fig. 2a presents the analyses of the Urbach tail energy that elucidate the imperfections in stoichiometric and surface defects. The corresponding tail energy values are 15.5, 14.6, and 14.6 meV for R-$FAPbI_3$, δ-$FAPbI_3$ and α-$FAPbI_3$, respectively. The highest tail energy of R-$FAPbI_3$ is due to the high absorption rate by free charge carriers inside the perovskite, which can be considered to have a high density of defects. In parallel, steady-state photoluminescence (PL) and time-resolved photoluminescence (TRPL) spectroscopy measurements were performed to evaluate the charge carrier properties of the $FAPbI_3$ films (Fig. 2b). As seen in Fig. S7, the α-$FAPbI_3$ film shows a stronger intensity than the other two samples (δ-$FAPbI_3$ and R-$FAPbI_3$), which indicates reduced nonradiative recombination in the α-$FAPbI_3$ films. The δ-$FAPbI_3$ and α-$FAPbI_3$ show both slower non-radiative recombination ($\tau_{1,\delta}$=53.52 ns, $\tau_{1,\alpha}$=53.53 ns) and radiative

recombination[53-54] ($\tau_{2,\delta}$=271.08 ns, $\tau_{2,\alpha}$=280.79 ns) than R-$FAPbI_3$ ($\tau_{1,R}$=50.09 ns, $\tau_{2,R}$=254.10 ns), which indicates the R-$FAPbI_3$ has more residual impurities than δ-$FAPbI_3$ and α-$FAPbI_3$ films. In addition, surface properties have a significant influence on the performance of the final devices because the loss of FAI cations and undercoordinated lead in the fabrication process are mainly located at the surface[19-20, 55-56]. The surface potential on the $FAPbI_3$ films was measured using Kelvin probe force microscopy (KPFM). The low surface roughness of the R-$FAPbI_3$, δ-$FAPbI_3$ and α-$FAPbI_3$ films (Fig. S8) indicates uniform grain size, which is beneficial for hole transport layer deposition. Moreover, the topography and contact potential difference (CPD) mapping of the δ-$FAPbI_3$ and α-$FAPbI_3$ films in Fig. S9 also exhibit a low average surface potential difference of 3.56 mV and 3.48 mV, which is substantially lower than that of R-$FAPbI_3$ (9.55 mV). This low surface potential is ascribed to the high crystallinity and no or little residue impurities at the grain boundaries, which is helpful for carrier extraction at the interface between perovskite and hole transport layer[57-58].

Figs. 2c-2d show current density-voltage (J-V) curves of PSCs and average PCEs based on 10 devices. For the R-$FAPbI_3$, the average J_{sc}, V_{oc}, FF and PCE are 23.37 mA/cm^2, 1.03 V, 0.777 and 18.62% in the case of the reverse scan (RS) and 23.34 mA/cm^2, 0.99 V, 0.739 and 17.12% in the case of the forward scan (FS), respectively (Table S4). The hysteresis index of R-$FAPbI_3$ (hysteresis index=PCE_{RS}/PCE_{FS}) is 1.09. In contrast, the PSCs based on δ-$FAPbI_3$ and α-$FAPbI_3$ show PCE_{RS} of 19.29% (J_{sc}=23.71 mA/cm^2, V_{oc}=1.03 V, FF=0.793) and 19.85% (J_{sc}=23.62 mA/cm^2, V_{oc}=1.05

V, FF=0.802), respectively. The corresponding PCE_{FS} of the δ-$FAPbI_3$ and α-$FAPbI_3$ based devices are 18.39% and 18.78%, respectively, which indicates reduced hysteresis indexes of 1.05 and 1.06 in comparsion with R-$FAPbI_3$. Based on Fig. 2c, it is worth noting that the variations in V_{oc} and FF in these three materials are significant, which corroborates the findings of significant trap density variations in Fig.s 2a-2b. In addition, a large spread of PCE values for R-$FAPbI_3$ (Fig. 2d) compared with δ-$FAPbI_3$ and α-$FAPbI_3$ indicates that the pre-synthesized δ-$FAPbI_3$ and α-$FAPbI_3$ can help lower variations of performance. Moreover, it is well known that short and long wavelength generate carriers close to the electron transport layer (ETL)/perovskite and perovskite/hole transport layer (HTL) interface, respectively[59-60]. The similar external quantum efficiency (EQE) values (Fig. S10) at the short wavelength region indicates that the same condition in terms of R-$FAPbI_3$, δ-$FAPbI_3$ and α-$FAPbI_3$ based PSCs. However, the traps/defects are predominantly at the top surface of the perovskite films and interface between perovskite and HTL instead of bulk films due to the generation of undercoordinated Pb and the loss of cations in the fabrication process[19-20, 55-56]. Therefore, a sharp edge at ~790 nm in the case of α-$FAPbI_3$ in the EQE spectrum (Fig. S10) indicates fewer traps/defects in the α-$FAPbI_3$ film[59-60].

Furthermore, the charge trap density values based on space-charge-limited current (SCLC) in the $FAPbI_3$ materials are determined by using the dark current voltage (I-V) measurement for a hole- and electron only devices with the architecture of ITO/PEDOT:PSS/perovskite/Au and ITO/SnO_2/perovskite/PCBM/Au (Fig. S11 and Table S5). When the applied voltage exceeds the first onset voltage, the current exhibits

a quick non-linear increase (n > 3), indicating that all traps are filled by the injected carriers. The applied voltage at the onset point is defined as the trap-filled limit voltage (V_{TFL}) which is correlated with the charge trap density[54, 61-62]

$$V_{TFL} = \frac{en_{trap}d^2}{2\varepsilon\varepsilon_0} \qquad (4)$$

where ε is the relative dielectric constant for $FAPbI_3$ (62.23)[47], d is the thickness of the perovskite layer (820 nm, see in Fig. S11b, inset), and ε_0 is the constant of vacuum permittivity in free space (8.8542×10^{-14} F/cm), e is electric charge (1.602×10^{-19} C) and V_{TFL} represents the onset voltage of the trap filled limit. As seen in Fig. S11 along with Table S5, V_{TFL} and n_{trap} in the hole-only device decreases from 0.754 V and 7.53 $\times 10^{15}$ cm^{-3} for the R-$FAPbI_3$ to 0.723 V and 7.23 $\times 10^{15}$ cm^{-3} for the δ-$FAPbI_3$, and 0.691 V and 6.9 $\times 10^{15}$ cm^{-3} for α-$FAPbI_3$. The electron-only devices showed a slight higher V_{TFL} (and n_{trap}) compared to that of hole-only devices, with 1.27 V (1.27 $\times 10^{16}$ cm^{-3}) for the R-$FAPbI_3$, 1.163 V (1.16 $\times 10^{16}$ cm^{-3}) for the δ-$FAPbI_3$, and 1.103 V (1.10 $\times 10^{16}$ cm^{-3}) for α-$FAPbI_3$. From the SCLC analysis, it is found that electron traps are dominant in the $FAPbI_3$ films[63-64]. The α-$FAPbI_3$ exhibit reduced electron traps, in agreement with their higher EQE values in the longer wavelength region as shown in Fig. S10, which indicates that the minimum defect density, dissolution and washing out of not well-crystallized precursors during the synthesis procedure help to generate high performing PSCs.

Additionally, the operational stability measurements (without encapsulation) was performed under AM 1.5 G illumination conditions in ambient (55% RH, 25 °C) (Fig.

2e). A fixed bias voltage was set to be the initial the maximum power point (MPP) voltage of PSCs[65-66]. It is well known that $FAPbI_3$ degrades quickly under high moisture without any encapsulation. To study the influences of these three $FAPbI_3$ materials on PSC operation stability, the high initial PCEs of 20.13%, 20.01% and 19.74% for α-$FAPbI_3$, R-$FAPbI_3$ and δ-$FAPbI_3$ PSCs were chosen. After continuous illumination, the devices of α-$FAPbI_3$, δ-$FAPbI_3$ and R-$FAPbI_3$ still kept 85.82%, 74.56% and 67.27% of their initial PCEs, respectively. These results suggest that the higher quality of synthesized precursors with less impurities and defects by the powder engineering strategy has a great impact on the long-term operational stability as well as photovoltaic performance.

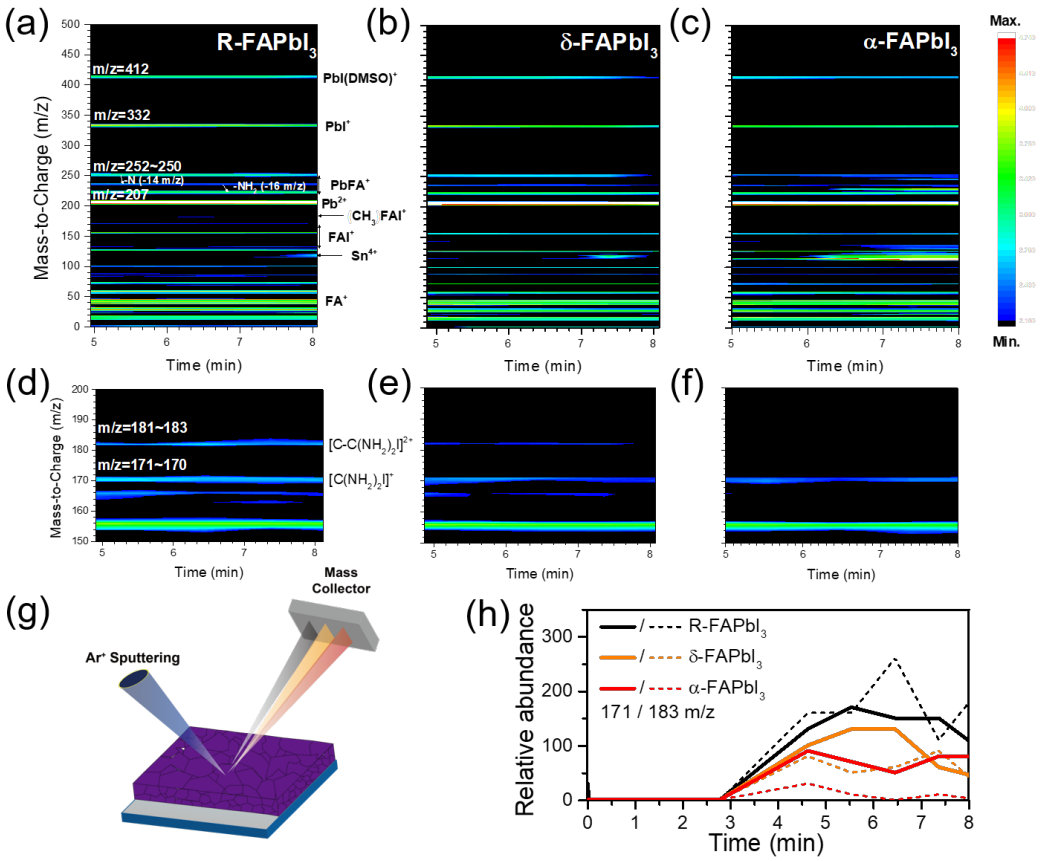

Fig. 3. Elemental visualization of the $FAPbI_3$ species based on the SIMS (positive ion

detection mode) depth profiles. (a, d) R-$FAPbI_3$; (b, e), δ-$FAPbI_3$; (c, f) α-$FAPbI_3$; (g) Simplified scheme presenting SIMS measurement; (h) Relative abundance as function of time of m/z = 171 amu (solid) and 183 amu (dash).

2.3. Elemental visualization of $FAPbI_3$ based on the SIMS depth profiles.

To identify the bulk chemical composition and the impurities in perovskite films (glass/SnO_2/perovskite), SIMS depth profiling (Fig. 3) was performed by sputtering the films with Ar^+ at 1 keV under ultra-high vacuum (10^{-9} Torr) (Fig. 3g). A myriad of positive fragments of $CH(NH_2)_2PbI_3$ films fabricated from different precursors were observed in Figs. 3a-3f. The first molecular ion peak at approximately 412 m/z is assigned to the fragments of PbI•DMSO (dimethylsulfoxide), which suggests that the DMSO is not evaporated completely because DMSO is strongly attached to PbI_2 and remains in the films even after heating at 150 ºC for 15 min. The peak intensity of PbI•DMSO in R-$FAPbI_3$ is one order of magnitude higher than that of α-$FAPbI_3$. The m/z = 332 amu is assigned to $[Pb\text{-}I]^+$, and the m/z bands between 252~250 amu and 207 amu (Pb^+) correspond to the $[(CH(NH_2)_2)Pb]^+$ parent molecule and its fragments. Figs. 3d-3f show enlarged element bands for m/z = 150 to 200 amu. The formamidinium iodide $[CH(NH_2)_2I]^+$ fragments between 170~171 amu is observed. In the case of R-$FAPbI_3$ and δ-$FAPbI_3$, additional bands at around 182-185 amu are observed, which are not related to the remaining solvents and or lead derivative elements. These fragment peaks are not iodine related compounds, to which a fragment of DMF (N,N-dimethylformamide) or DMSO is bound. These bands are assigned to 185 amu = $[C_2H_3(NH_2)_2I]^+$ ~ 183 amu = $[C_2(NH_2)_2I]^+$. The amount of these elements (m/z = 182-185 amu) decreases from R-$FAPbI_3$ to α-$FAPbI_3$ (Figs. 3d-3f). Moreover, these bands

can be observed with a higher concentration in the bulk than at the surface (Fig. 3h). These bands originate from agglomerated non-reacted FAI inside the bulk of perovskite film. It demonstrates that the formation of $FAPbI_3$ is not fully processed due to the evaporation of the solvents during the post-annealing. Due to a large solubility gap between PbI_2 and FAI, unreacted FAI can be formed inside the perovskite film, which acts as an electrical resistance between grains for the photogenerated free carriers leading to the V_{oc} losses in PSCs (Fig. 2c).

Further detailed analysis of molecular peaks between 0-80 m/z leads to the observation of DMF parent molecule and its fragments (73~28 amu). The relative amount of residual DMF in R-$FAPbI_3$ is higher than δ-$FAPbI_3$ and α-$FAPbI_3$. Though the boiling point of DMF (153 ºC) is relatively lower than DMSO (189 ºC), it is still inside the perovskite film, which can be a major influence on the operational stability. The individual DMSO molecule (m/z = 78 amu) is not observed in our SIMS profiles, but it appears always combined with lead. DMSO and DMF are the most frequently used solvents in the perovskite field, and they are one of the factors that lead to degradation during solar cell operation. The formamidinium cation FA^+ (=$CH_5N_2^+$) parent molecule appears at m/z = 45 amu and its fragments between 45 ~ 28 amu. The m/z = 41 amu assigned as CHN_2^+ (=41 m/z) is higher in R-$FAPbI_3$ than in δ-$FAPbI_3$ and α-$FAPbI_3$. The magnitude of this peak varies depending on the quality of the materials and/or method of synthesis. Imperfection of stoichiometry by residual FAI inside the $FAPbI_3$ perovskite not only degrades the photovoltaic performance but also hinders the vaporization of residual solvent during the annealing process, which

influences the overall $FAPbI_3$ PSC operational stability.

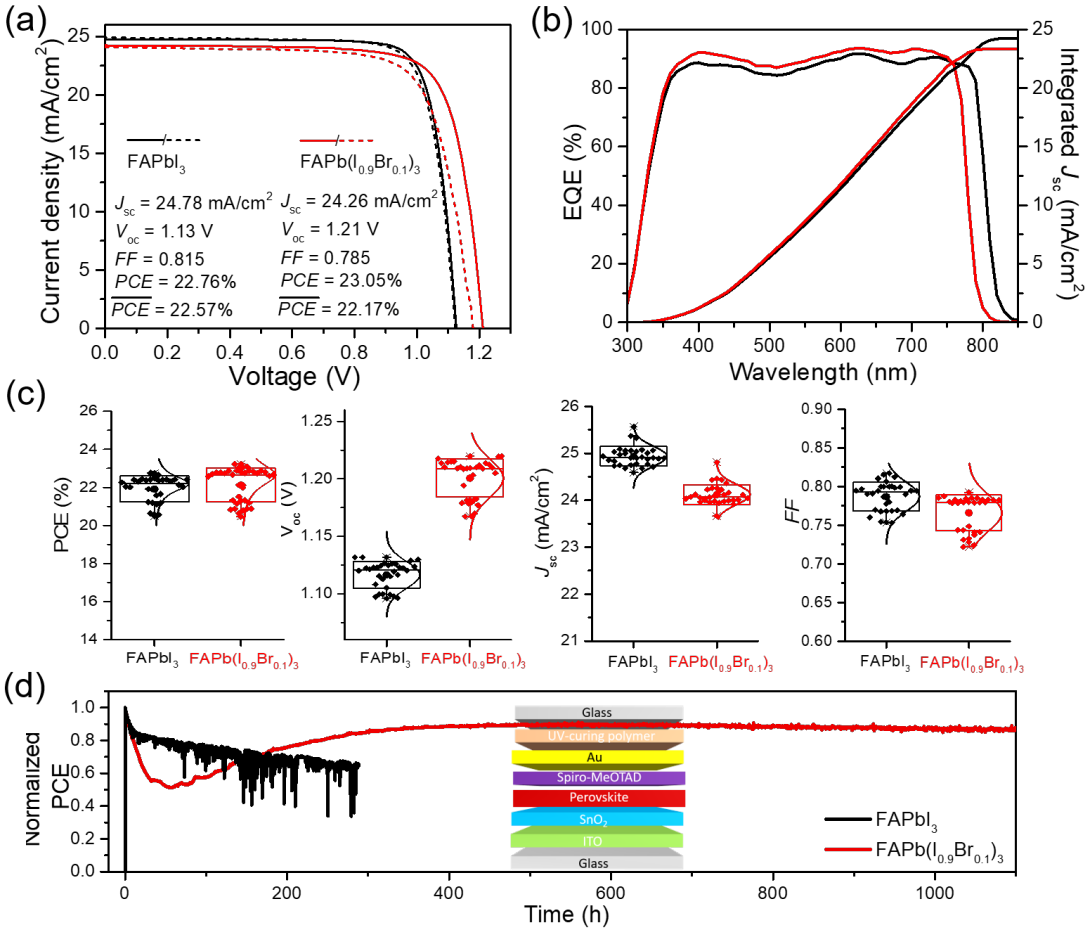

Fig. 4. (a) Current density-voltage (J-V) curves of the best-performing α-$FAPbI_3$ and $FAPb(I_{0.9}Br_{0.1})_3$ based perovskite solar cells using PEAI. Average performance values are shown as inset; (b) The corresponding external quantum efficiency and integrated J_{sc} of α-$FAPbI_3$ and $FAPb(I_{0.9}Br_{0.1})_3$; (c) PCE, V_{oc}, J_{sc} and FF values obtained from 16 devices of α-$FAPbI_3$ and $FAPb(I_{0.9}Br_{0.1})_3$ based perovskite solar cells; (d) Operational stability measurements of encapsulated α-$FAPbI_3$ and $FAPb(I_{0.9}Br_{0.1})_3$ devices under a steady voltage output and continuous AM 1.5G illumination without UV cutoff filter in ambient (55% RH, 25 °C). Inset shows the schematic illustration of the encapsulated device.

2.4. PSC performance with surface passivation.

Based on the above findings, we have confirmed that our pre-synthetized $FAPbI_3$

powder precursors by powder engineering led to high efficiency and better stability by effectively eliminating the residual compositions resulting in a high crystallinity perovskites. Two additional strategies were implemented to further boost up efficiency and operational stability: (i) the phenethylammonium iodide (PEAI) treatment on the surface to passivate the surface defects[67]; and (ii) substitution of I by a smaller ion for Br to form the mixed-halide $FAPb(I_{0.9}Br_{0.1})_3$ perovskite, which favors the formation of the cubic structures and improves operational stability[11]. As shown in Fig. 4a, for the best performing α-$FAPbI_3$ PSC with the PEAI treatment, we attained an average PCE of 22.57% (PCE=22.76%, J_{sc}=24.78 mA/cm^2, V_{oc}=1.13 V, FF=0.815 for reverse scan; PCE=22.38%, J_{sc}=24.91 mA/cm^2, V_{oc}=1.12 V, FF=0.800 for forward scan). As comparison, the PEAI treated $FAPb(I_{0.9}Br_{0.1})_3$ based PSC generated only a slightly lower average PCE of 22.17% (PCE=23.05%, J_{sc}=24.26 mA/cm^2, V_{oc}=1.21 V, FF=0.785 for reverse scan, and PCE=21.29%, J_{sc}=24.12 mA/cm^2, V_{oc}=1.18 V, FF=0.749 for forward scan). It is notable that an average V_{oc} of 1.19 V is achieved by adding 10% of $FAPbBr_3$ with the surface treatment of PEAI. The hysteresis index was 1.017 for α-$FAPbI_3$ and 1.082 for $FAPb(I_{0.9}Br_{0.1})_3$. EQE measurements showed a high quantum yield throughout the entire wavelength range (Fig. 4b), leading to an integrated photocurrent density of 24.25 and 23.35 mA/cm^2 for α-$FAPbI_3$ and $FAPb(I_{0.9}Br_{0.1})_3$, respectively. Statistical analyses of the photovoltaic parameters from 16 devices reveal that the performance is reproducible with minimal variations (Fig. 4c). Therefore, our strategy of FA-perovskite synthesis is effective in improving the stoichiometry, thereby leading to a considerable enhancement in PCE.

Next, we investigated the operational stability of α-$FAPbI_3$ and $FAPb(I_{0.9}Br_{0.1})_3$ devices encapsulated with an UV-curing polymer (Fig. 4d, inset). The continuous operational stability of α-$FAPbI_3$ and $FAPb(I_{0.9}Br_{0.1})_3$ devices encapsulated with an UV-curing polymer were performed by recording the devices power output under a steady voltage output and one sun illumination in ambient conditions (Fig. 4d). It is known that there are two kinds of decay behaviors in the operational stability profiles of PSCs. One is the fast initial exponential decay, which can be recovered. The other decay is the linear one, which is irreversible and associated with the permanent degradation process[65, 68]. In the $FAPbI_3$ perovskites, FA cation can be decompose to acid-base decomposition (formamidine + HI) and/or HCN + NH_3 and PbI_2 is prone to release Pb^0 and I_2 gas[69]. It is worth noting that all of above degradation reactions are reversible. The α-$FAPbI_3$ based PSC showed the characteristic 2-stage degradation processes[65, 68], i.e., a fast decay that began at about 30 min after starting the test, followed by a slow permanent decay that took place for about 13-14 hours. The PCE continuously decreased and eventually reached ~60% of the initial PCE after about 280 hours. In contrast, the mixed halide $FAPb(I_{0.9}Br_{0.1})_3$ perovskite showed an operation stability profile with enhanced stability maintaining 88% of the initial PCE even after 1200 hours. The fast burn-in decay process in the first 300 hours is possibly associated with the thermal effect because the continuous light illumination would generate iodine, which induces a faster perovskite degradation[24-25]. In addition, the encapsulated PSCs can be regarded as a closed system, and once the released FA cation and I_2 gas reach a certain concertation, it leads to a thermodynamic equilibrium between

perovskite and I_2. In this case, the degradation of perovskite is retarded[24-25, 61]. More discussions can be found in Supplementary Note. Therefore, a slight increase of the performance after the burn-in decay is likely a result of the recovery of the perovskite film, which is consistence with previous operational stability results[11, 61]. Finally, a slow decay of the performance with a slope of approximately -0.01%/h follows after the burn-in loss, which corresponds to a T_{80} lifetime over 2000 h.

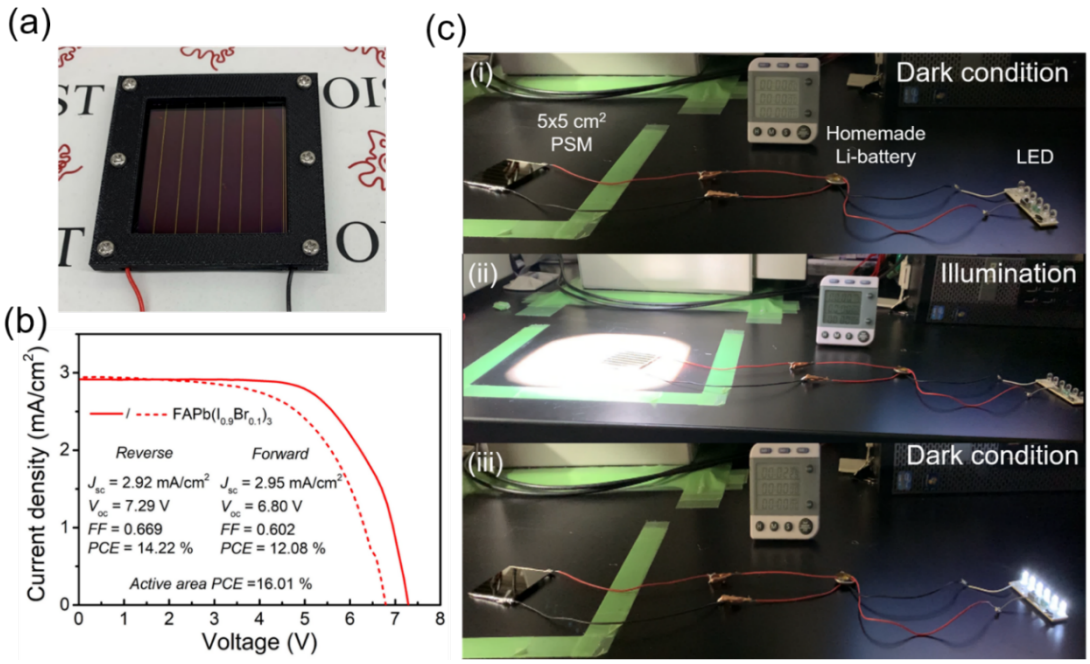

Fig. 5. (a) Photo of a 5×5 cm^2 PSM; (b) J-V curves of the best-performing 5×5 cm^2 PSM under reverse and forward scan direction; (c) Photos showing the operation of a proof-of-concept perovskite solar module-lithium ion battery-light-emitting diode (PSM-LIB-LED) device.

2.5. Proof of concept, Solar module-lithium ion battery-light emitting diode.

We have also performed some proof of concept experiments to evaluate the upscalability of this method. A 5 cm × 5 cm ITO substrate consisting of seven sub-cells was used as the substrate with a designed area of 22.4 cm^2 (Fig. 5a and Fig. S12a).

Often it is found that the efficiency drops when upscaling devices from lab-scale PSCs to larger-size PSMs. This efficiency decrease can be ascribed to the following factors:[70-72] (i) amplified effects of imperfections such as defects, impurities and pinholes in the perovskite films of larger size solar cell devices, which leads to higher carrier recombination; (ii) the increase of the series resistance of transparent conductive oxides (i.e., ITO substrates and the SnO_2 layer). Based on the above findings that the pre-synthesized perovskite powder not only has high crystallinity, but also reduces the residue solvent and unreacted intermediate chemical compositions, which can reduce the amplified effects of imperfections as discussed in (i) above. The same α-$FAPbI_3$ and $FAPbBr_3$ pre-synthesized powders were used to fabricate the perovskite solar modules (PSMs) with a configuration of ITO/SnO_2/$FAPb(I_{0.9}Br_{0.1})_3$/Spiro-MeOTAD/Au (Figs. S12b-12c). The champion module PCE of 14.22% was obtained with a V_{oc} of 7.29 V, J_{sc} of 2.92 mA/cm^2 and FF of 0.669 under reverse scan as seen in Fig. 5b. The resultant active area PCE up to 16.01% was achieved with a geometric fill factor of 0.888 (Fig. S13)[61]. Furthermore, statistical analyses of the performance based on 10-PSMs gave an average PCE of 12.45% ± 1.27% (Fig. S14 and Table S6), which indicated the good upscalability of this method. Furthermore, a proof-of-concept perovskite solar module-lithium ion battery-light-emitting diode (PSM-LIB-LED) device was fabricated as shown in Fig. 5c and Supplementary Video. Initially, a homemade LIB (See in method) was fully discharged and could not power the LED to work under dark condition (step i). Then the PSM was illuminated under a solar simulator (1 sun), which is able to charge the LIB (step ii). After 2 min illumination, the solar simulator was turned off

and LED was switched on. As we can see in Fig. 5c (step iii), the LED started to give off a strong light. This simple PSM-LiB-LED device exemplifies the promising integration capability of our PSM with various other functional devices in the future.

3. Conclusions

We successfully synthesized highly crystalline phase pure δ-$FAPbI_3$ and α-$FAPbI_3$ powders with almost no unwanted intermediate chemical compositions (i.e., the unreacted phases and residual solvent) by a simple powder engineering method. Employing SIMS depth profiling, unreacted molecules at 182–183 m/z and PbI•DMSO at 412 m/z were detected in the films, which may have detrimental effects on the efficiency and operational stability of PSCs. Perovskite films prepared by α-$FAPbI_3$ crystalline powders showed a substantial reduction of these aggregates compared to δ-$FAPbI_3$ and R-$FAPbI_3$ films. The best efficiency of 22.76% for α-$FAPbI_3$ and 23.05% for $FAPb(I_{0.9}Br_{0.1})_3$ were achieved using pre-synthesized powders via the powder engineering method. The continuous operational stability of the $FAPb(I_{0.9}Br_{0.1})_3$ PSC still maintained ＞88% at 1200 h with T_{80} over 2000 h. Furthermore, our 5 × 5 cm^2 PSM achieved a PCE of 14.22% (active area PCE of 16.01%) and the pre-synthesized powder strategy also showed great potential for upscaling. A simple proof-of-concept PSM-LIB-LED device was demonstrated, which exemplifies the integration capability of our PSM with other functional devices in the future.

Acknowledgements

This work was supported by funding from the Energy Materials and Surface Sciences Unit of the Okinawa Institute of Science and Technology Graduate University, the OIST R&D Cluster Research Program, and the OIST Proof of Concept (POC) Program. We thank the OIST Micro/Nanofabrication Section and Imaging Section for the support.

Appendix A. Supplementary data

Supplementary data to this article can be found online at https://doi.org/10.1016/j.nanoen.XXXX.

References:

[1] A. Kojima, K. Teshima, Y. Shirai, T. Miyasaka, J. Am. Chem. Soc. 131 (2009) 6050-6051.

[2] J. H. Im, C. R. Lee, J. W. Lee, S. W. Park, N. G. Park, Nanoscale 3 (2011) 4088-4093.

[3] Best research-cell efficiencies. https://www.nrel.gov/pv/assets/pdfs/best-research-cell-efficiencies.20201228.pdf. (accessed by January, 2021)

[4] M. A. D. Green, E. D. Dunlop, J. Hohl-Ebinger, M. Yoshita, N. Kopidakis, A. W. Y. Ho-Baillie, Prog. Photovolt. 28 (2020) 3-15.

[5] S.-H. Turren-Cruz, A. Hagfeldt, M. Saliba, Science 362 (2018) 449-453.

[6] H. Lu, Y. Liu, P. Ahlawat, A. Mishra, W. R. Tress, F. T. Eickemeyer, Y. Yang, F. Fu, Z. Wang, C. E. Avalos, B. I. Carlsen, A. Agarwalla, X. Zhang, X. Li, Y. Zhan, S. M. Zakeeruddin, L. Emsley, U. Rothlisberger, L. Zheng, A. Hagfeldt, M. Gratzel, Science 370 (2020) eabb8985.

[7] G. Kim, H. Min, K. S. Lee, D. Y. Lee, S. M. Yoon, S. Il Seok, Science 370 (2020) 108-112.

[8] C. Yi, J. Luo, S. Meloni, A. Boziki, N. Ashari-Astani, C. Grätzel, S. M. Zakeeruddin, U. Röthlisberger, M. Grätzel, Energy Environ. Sci. 9 (2016) 656-662.

[9] P. Wang, R. Li, B. Chen, F. Hou, J. Zhang, Y. Zhao, X. Zhang, Adv. Mater. 32 (2020), 1905766.

[10] G. Tong, H. Li, G. Li, T. Zhang, C. Li, L. Yu, J. Xu, Y. Jiang, Y. Shi, K. Chen, Nano Energy 48 (2018) 536-542.

[11] E. H. Jung, N. J. Jeon, E. Y. Park, C. S. Moon, T. J. Shin, T. Y. Yang, J. H. Noh, J. Seo, Nature 567 (2019) 511-515.

[12] S. You, H. Zeng, Z. Ku, X. Wang, Z. Wang, Y. Rong, Y. Zhao, X. Zheng, L. Luo, L. Li, S. Zhang, M. Li, X. Gao, X. Li, Adv. Mater. 32 (2020) 2003990.

[13] H. Zhu, Y. Liu, F. T. Eickemeyer, L. Pan, D. Ren, M. A. Ruiz-Preciado, B. Carlsen, B. Yang, X. Dong, Z. Wang, H. Liu, S. Wang, S. M. Zakeeruddin, A.

Hagfeldt, M. I. Dar, X. Li, M. Gratzel, Adv. Mater. 32 (2020) 1907757.

[14] M. A. Mahmud, T. Duong, Y. Yin, J. Peng, Y. Wu, T. Lu, H. T. Pham, H. Shen, D. Walter, H. T. Nguyen, N. Mozaffari, G. D. Tabi, Y. Liu, G. Andersson, K. R. Catchpole, K. J. Weber, T. P. White, Small 16 (2020) 2005022.

[15] T. S. Su, F. T. Eickemeyer, M. A. Hope, F. Jahanbakhshi, M. Mladenovic, J. Li, Z. Zhou, A. Mishra, J. H. Yum, D. Ren, A. Krishna, O. Ouellette, T. C. Wei, H. Zhou, H. H. Huang, M. D. Mensi, K. Sivula, S. M. Zakeeruddin, J. V. Milic, A. Hagfeldt, U. Rothlisberger, L. Emsley, H. Zhang, M. Gratzel, J. Am. Chem. Soc. 142 (2020) 19980-19991.

[16] N. J. Jeon, H. Na, E. H. Jung, T.-Y. Yang, Y. G. Lee, G. Kim, H.-W. Shin, S. Il Seok, J. Lee, J. Seo, Nat. Energy 3 (2018) 682-689.

[17] X. Zhu, M. Du, J. Feng, H. Wang, Z. Xu, L. Wang, S. Zuo, C. Wang, Z. Wang, C. Zhang, X. Ren, S. Priya, D. Yang, S. F. Liu, Angew. Chem. Int. Ed. 60, (2021) 4238-4244.

[18] G. Tong, M. Jiang, D. Y. Son, L. K. Ono, Y. B. Qi, Adv. Funct. Mater. 30 (2020) 2002526.

[19] D. Meggiolaro, E. Mosconi, F. De Angelis, ACS Energy Lett. 4 (2019) 779-785.

[20] L. K. Ono, S. F. Liu, Y. B. Qi, Angew.Chem. Int. Ed. 59 (2020) 6676.

[21] Q. Chen, H. Zhou, T.-B. Song, S. Luo, Z. Hong, H.-S. Duan, L. Dou, Y. Liu, Y. Yang, Nano Lett. 14 (2014) 4158-4163.

[22] Y. Zhao, Q. Li, W. Zhou, Y. Hou, Y. Zhao, R. Fu, D. Yu, X. Liu, Q. Zhao, Sol. RRL 3 (2019) 1800296.

[23] J. Euvrard, O, Gunawan, D. B. Mitzi, Adv. Energy Mater. 9 (2019), 1902706.

[24] E. J. Juarez-Perez, L. K. Ono, M. Maeda, Y. Jiang, Z. Hawash, Y. B. Qi, J. Mater. Chem. A 6 (2018) 9604-9612.

[25] S. Wang, Y. Jiang, E. J. Juarez-Perez, L. K. Ono, Y. B. Qi, Nat. Energy 2 (2016) 16195.

[26] G. Tumen-Ulzii, C. Qin, D. Klotz, M. Leyden, P. Wang, M. Auffray, T. Fujihara, T. Matsushima, J. Lee, S. Lee, Y. Yang, C. Adachi, Adv. Mater. 32 (2020) 1905035

[27] T. Du, J. Kim, J. Ngiam, S. Xu, P. R. F. Barnes, J. R. Durrant, M. A. McLachlan, Adv. Funct. Mater. 28 (2018) 1801808.

[28] D.-Y. Son, J.-W. Lee, Y. J. Choi, I.-H. Jang, S. Lee, P. J. Yoo, H. Shin, N. Ahn, M. Choi, D. Kim, N.-G. Park, Nat. Energy 1 (2016) 16081.

[29] Z. Hawash, S. R. Raga, D.-Y. Son, L. K. Ono, N.-G. Park, Y. B. Qi, J. Phys. Chem. Lett. 8 (2017) 3947-3953.

[30] Z. Wang, Y. Zhou, S. Pang, Z. Xiao, J. Zhang, W. Chai, H. Xu, Z. Liu, N. P. Padture, G. Cui, Chem. Mater. 27 (2015) 7149-7155.

[31] B. Chen, Z. Yu, K. Liu, X. Zheng, Y. Liu, J. Shi, D. Spronk, P. N. Rudd, Z. Holman, J. Huang, Joule 3 (2019) 177-190.

[32] G. Pellegrino, S. Colella, I. Deretzis, G.G. Condorelli, E. Smecca, G. Gigli, A. La Magna, A. Alberti, J. Phys. Chem. C 119 (2015) 19808-19816.

[33] H. Wei, Y. Fang, P. Mulligan, W. Chuirazzi, H.-H. Fang, C. Wang, B. R. Ecker, Y. Gao, M. A. Loi, L. Cao, J. Huang, Nat. Photonics 10 (2016) 333-339.

[34] Y. C. Kim, K. H. Kim, D. Y. Son, D. N. Jeong, J. Y. Seo, Y. S. Choi, I. T. Han, S. Y. Lee, N. G. Park, Nature 550 (2017) 87-91.

[35] Y. Song, W. Bi, A. Wang, X. Liu, Y. Kang, Q. Dong, Nat. Commun. 11 (2020) 274.

[36] Y. Liu, Y. Zhang, Z. Yang, J. Feng, Z. Xu, Q. Li, M. Hu, H. Ye, X. Zhang, M. Liu, K. Zhao, S. F. Liu, Mater. Today 22 (2019) 67-75.

[37] W. G. Li, X. D. Wang, J. F. Liao, Y. Jiang, D. B. Kuang, Adv. Funct. Mater. 30 (2020) 1909701.

[38] A. Y. Alsalloum, B. Turedi, X. Zheng, S. Mitra, A. A. Zhumekenov, K. J. Lee, P. Maity, I. Gereige, A. AlSaggaf, I. S. Roqan, O. F. Mohammed, O. M. Bakr, ACS Energy Lett. 5 (2020) 657-662.

[39] Z. Chen, B. Turedi, A. Y. Alsalloum, C. Yang, X. Zheng, I. Gereige, A. AlSaggaf, O. F. Mohammed, O. M. Bakr, ACS Energy Lett. 4 (2019) 1258-1259.

[40] Y. Lei, Y. Chen, R. Zhang, Y. Li, Q. Yan, S. Lee, Y. Yu, H. Tsai, W. Choi, K. Wang, Y. Luo, Y. Gu, X. Zheng, C. Wang, C. Wang, H. Hu, Y. Li, B. Qi, M. Lin, Z. Zhang, S. A. Dayeh, M. Pharr, D. P. Fenning, Y. H. Lo, J. Luo, K. Yang, J.

Yoo, W. Nie, S. Xu, Nature 583 (2020) 790-795.

[41] X. Cheng, S. Yang, B. Cao, X. Tao, Z. Chen, Adv. Funct. Mater. 30 (2019) 1905021.

[42] Y. Zhang, S. Seo, S. Y. Lim, Y. Kim, S.-G. Kim, D.-K. Lee, S.-H. Lee, H. Shin, H. Cheong, N.-G. Park, ACS Energy Lett. 5 (2019) 360-366.

[43] S. A. Fateev, A. A. Petrov, V. N. Khrustalev, P. V. Dorovatovskii, Y. V. Zubavichus, E. A. Goodilin, A. B. Tarasov, Chem. Mater. 30 (2018) 5237-5244.

[44] M. I. Saidaminov, A. L. Abdelhady, G. Maculan, O. M. Bakr, Chem. Commun. 51 (2015) 17658-17661.

[45] M. I. Saidaminov, A. L. Abdelhady, B. Murali, E. Alarousu, V. M. Burlakov, W. Peng, I. Dursun, L. Wang, Y. He, G. Maculan, A. Goriely, T. Wu, O. F. Mohammed, O. M. Bakr, Nat. Commun. 6 (2015) 7586.

[46] J. M. Kadro, K. Nonomura, D. Gachet, M. Gratzel, A. Hagfeldt, Sci. Rep. 5 (2015) 11654.

[47] Y. Liu, J. Sun, Z. Yang, D. Yang, X. Ren, H. Xu, Z. Yang, S. F. Liu, Adv. Optical Mater. 4 (2016) 1829.

[48] A. A. Coelho, J. Appl. Crystallogr. 51 (2018) 210-218.

[49] M. T. Weller, O. J. Weber, J. M. Frost, A. Walsh, J. Phys. Chem. Lett. 6 (2015) 3209-3212.

[50] C. C. Stoumpos, C. D. Malliakas, M. G. Kanatzidis, Inorg. Chem. 52 (2013) 9019-9038.

[51] N. J. Jeon, J. H. Noh, Y. C. Kim, W. S. Yang, S. Ryu, S. Il. Seok, Nat. Mater. 13 (2014) 897-903.

[52] M. Kim, G.-H. Kim, T. K. Lee, I. W. Choi, H. W. Choi, Y. Jo, Y. J. Yoon, J. W. Kim, J. Lee, D. Huh, H. Lee, S. K. Kwak, J. Y. Kim, D. S. Kim, Joule 3 (2019) 2179-2192.

[53] G. Tong, M. Jiang, D.-Y. Son, L. Qiu, Z. Liu, L. K. Ono, Y. B. Qi, ACS Appl. Mater. Interfaces 12 (2020) 14185-14194.

[54] G. Tong, T. Chen, H. Li, L. Qiu, Z. Liu, Y. Dang, W. Song, L. K.Ono, Y. Jiang,

Y. B. Qi, Nano Energy 65 (2019) 104015.

[55] Z. Wu, M. Jiang, Z. Liu, A. Jamshaid, L. K. Ono, Y. B. Qi, Adv. Energy Mater. 10 (2020) 1903696.

[56] J. Yang, Q. Cao, Z. He, X. Pu, T. Li, B. Gao, X. Li, Nano Energy, 82 (2021) 105731.

[57] Y. Zhou, L. Wang, S. Chen, S. Qin, X. Liu, J. Chen, D.-J. Xue, M. Luo, Y. Cao, Y. Cheng, E. H. Sargent, J. Tang, Nat. Photonics 9 (2015) 409-415.

[58] J. S. Yun, A. Ho-Baillie, S. Huang, S. H. Woo, Y. Heo, J. Seidel, F. Huang, Y. B. Cheng, M. A. Green, J. Phys. Chem. Lett. 6 (2015) 875-880.

[59] T. Bu, L. Wu, X. Liu, X. Yang, P. Zhou, X. Yu, T. Qin, J. Shi, S. Wang, S. Li, Z. Ku, Y. Peng, F. Huang, Q. Meng, Y.-B. Cheng, J. Zhong, Adv. Energy Mater. 7 (2017) 1700576.

[60] G. Tong, D.-Y. S, L. K. Ono, Y. Liu, Y. Hu, H. Zhang, A. Jamshaid, L. Qiu, Z. Liu, Y. B. Qi, Adv. Energy Mater. 11 (2021) 2003712.

[61] Z. Liu, L. Qiu, L. K. Ono, S. He, Z. Hu, M. Jiang, G. Tong, Z. Wu, Y. Jiang, D.-Y. Son, Y. Dang, S. Kazaoui, Y. B. Qi, Nat. Energy 5 (2020) 596-604.

[62] M. Li, T. Sun, J. Shao, Y. Wang, J. Hu, Y. Zhong, Nano Energy, 79 (2021) 105462.

[63] Q. Dong, Y. Fang, Y. Shao, P. Mulligan, J. Qiu, L. Cao, J. Huang Science 347 (2015) 967-970.

[64] Y. Zhao, H. Tan, H. Yuan, Z. Yang, J. Z. Fan, J. Kim, O. Voznyy, X. Gong, L. N. Quan, C. S. Tan, J. Hofkens, D. Yu, Q. Zhao, E. H. Sargent, Nat. Commun. 9 (2018) 1607.

[65] K. Domanski, E. A. Alharbi, A. Hagfeldt, M. Grätzel, W. Tress, Nat. Energy 3 (2018) 61-67.

[66] M. V. Khenkin, E. A. Katz, A. Abate, G. Bardizza, J. J. Berry, C. Brabec, F. Brunetti, V. Bulović, Q. Burlingame, A. Di Carlo, R. Cheacharoen, Y.-B. Cheng, A. Colsmann, S. Cros, K. Domanski, M. Dusza, C. J. Fell, S. R. Forrest, Y. Galagan, D. Di Girolamo, M. Grätzel, A. Hagfeldt, E. von Hauff, H. Hoppe, J.

Kettle, H. Köbler, M. S. Leite, S. Liu, Y.-L. Loo, J. M. Luther, et al., Nat. Energy 5 (2020) 35-49.

[67] Q. Jiang, Y. Zhao, X. Zhang, X. Yang, Y. Chen, Z. Chu, Q. Ye, X. Li, Z. Yin, J. You, Nat. Photonics 13 (2019) 460-466.

[68] L. K. Ono, Y. B. Qi, S. F. Liu, Joule 2 (2018) 1961-1990.

[69] E. J. Juarez-Perez, L. K. Ono, Y. B. Qi, J. Mater. Chem. A 7 (2019) 16912-16919.

[70] D. H. Kim, J. B. Whitaker, Z. Li, M. F. A. M. van Hest, K. Zhu, Joule 2 (2018) 1437-1451.

[71] L. Qiu, S. He, L. K. Ono, S. F. Liu, Y. B. Qi, ACS Energy Lett. 4 (2019) 2147-2167.

[72] J. Werner, C. C. Boyd, T. Moot, E. J. Wolf, R. M. France, S. A. Johnson, M. F. A. M. van Hest, J. M. Luther, K. Zhu, J. J. Berry, M. D. McGehee, Energy Environ. Sci. 13 (2020) 3393-3403.